Inorganic Chemistry

pubs.acs.org/IC
Article

Secondary Coordination Sphere Effects in Macrocycle-Embedded Mononuclear Ru(bda) Water Oxidation Catalysts

Gourab Das, Daniel A. P. Friedewald, Deqi Tang, Kazutaka Shoyama, Fabrizio Creazzo, Sandra Luber,* and Frank Würthner*

Cite This: *Inorg. Chem.* 2026, 65, 4710−4720

ABSTRACT: Integration of Ru(bda) [bda = (2,2’-bipyridine)-6,6’-dicarboxylate] water oxidation catalysts together with dibenzofuran, dibenzothiophene, or carbazole heterocycles within macrocycles **1**-**3** affords structures with different conformational preferences. The latter are dictated by noncovalent interactions of the bda oxygens with NH (hydrogen bond) or S (chalcogen bond). The different orientations afford changes in the secondary coordination sphere, thereby influencing the rate and mechanism of photocatalytic water oxidation for the three mononuclear Ru(bda)-based catalysts, with the dibenzothiophene- and carbazole-based ones favoring the unimolecular pathway (first-order kinetics), typically related to water nucleophilic attack (WNA), and the dibenzofuran one operating via a bimolecular pathway (second-order kinetics), typically related to the interaction of two metal-oxo species (I2M). NMR and single crystal X-ray analyses provided insight into the conformational preferences of the precursor macrocycles in the Ru(II) state. Photocatalytic studies including the H/D kinetic isotope effect (KIE) in deuterated water together with theoretical studies on the orientation angle-dependent energy profile for macrocycles in the Ru(V) state afforded a structure−property relationship that explains the outcome of the water oxidation experiments.

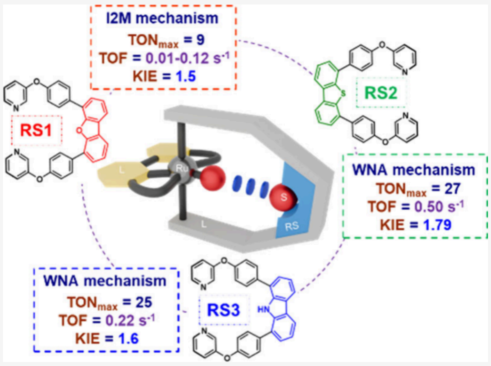

1. INTRODUCTION

Global warming and environmental pollution require the search for alternative sustainable energy sources[1,2] that are in the most ideal scenario based on widely abundant natural resources such as sunlight, air and water, thereby reducing the dependency on fossil fuels.[3,4] Photosynthesis provides a blueprint for harvesting solar energy and conversion of water and carbon dioxide into energy-rich organic compounds and oxygen.[5−8] However, taking inspiration from the oxygen-evolving complex[9−11] of photosystem II (OEC-PSII) for the design of catalysts for use in artificial photosynthesis remains a major challenge. The activity of these catalysts strongly depends on the anodic half-cell reaction, which involves the challenging four-electron oxidation of water to molecular oxygen ($2H_2O \rightarrow O_2 + 4e^- + 4H^+$).[12−16] Several transition metal-based catalysts have been developed for successful water oxidation with low overpotentials, high turnover frequency (TOF) and turnover number (TON),[15,16] which, however, often rely on complex multinuclear architectures similar to the natural $CaMn_4O_5(H_2O)_4$ cluster found in OEC-PSII.[17,18]

In this regard, second row Ru-based transition metal catalysts with a larger electron reservoir stand out. For Ru WOCs, after a rather long induction period following the pioneering “blue dimer” discovery by Meyer,[19] during the last two decades a variety of binuclear and even mononuclear catalysts with high TOF and TON became available.[20−41] Initial examples for mononuclear catalysts operated via the diffusion-controlled interaction of two $Ru^V{=}O$ species (I2M mechanism),[24−29] thereby again relying on two metal centers and enabling high turnover frequencies (TOFs) only at high catalyst concentrations in solution, thereby being less suitable for photo- and electrocatalytic operation of surface-bound catalysts.

For this reason, the discovery of second coordination sphere effects supporting the water nucleophilic attack (WNA) to $Ru^V{=}O$ became important.[30−41] The presence of a suitable coordination sphere around the metal center may support the formation of water networks for the promotion of WNA by proton-coupled electron transfer steps,[37−41] similar as observed ubiquitously in enzymatic pockets including those observed in OEC-PSII.[9−11] However, the design of a suitable second coordination sphere is far more challenging than for the first coordination sphere. For this reason, it is not surprising that initial improvements for mononuclear Ru WOCs originated from the optimization of the first coordination sphere. Thus,

Received: December 19, 2025
Revised: January 29, 2026
Accepted: February 4, 2026
Published: February 18, 2026

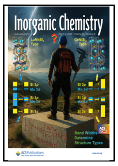

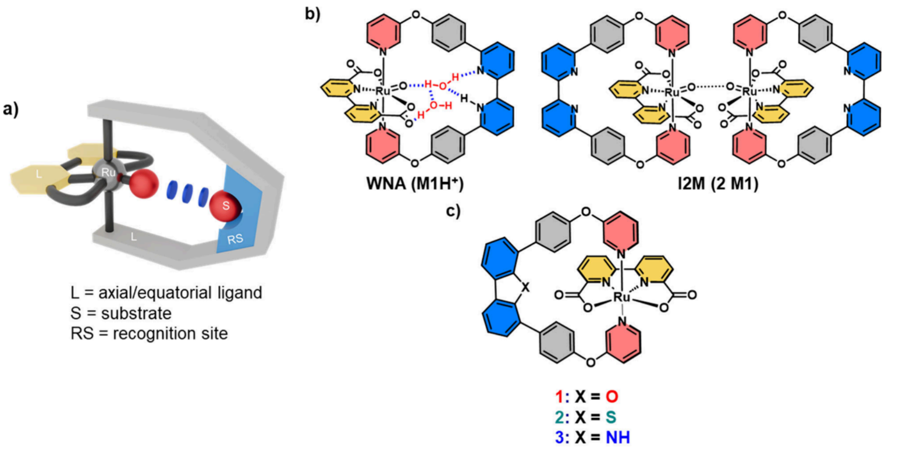

Figure 1. (a) Concept for the creation of synthetic enzyme-like pockets for organizing substrate water molecules in front of a catalytic Ru^{V}=O center and (b) previously studied pH-dependent Ru(bda) catalyst **M1** and (c) here investigated Ru catalysts **1**-**3**.

following the discovery of mononuclear Ru WOCs with 4-*tert*-butyl-2,6-di(1,8-naphthyridin-2-yl)pyridine as the primary coordination sphere by Thummel in 2005,[26] Sun and co-workers introduced the 2,2'-bipyridine-6,6'-dicarboxylate (bda) ligand which as a four-coordinate equatorial ligand provides two negative charges that perfectly compensate the hole accumulation on the Ru center at higher oxidation states and enables the coordination of a seventh oxo ligand in the equatorial plane.[28] From there on, upon further variations by other equatorial ligands such as 2,2':6,2-terpyridine-6,6"-dicarboxylate (tda), 2,2'-bipyridine-6,6'-diylbis(hydrogen phosphonate) (bpaH) or 2,2'-bipyridine-6,6'-disulfonate (bds) second coordination sphere effects were recognized, e.g. by dangling carboxylate groups or other noncovalent interactions from substituents in close vicinity to the Ru^{V}=O center supporting the nucleophilic water attack.[30−36]

The entry of our group into this research field came from another perspective, i.e. the hypothesis that well-organized water networks in front of the Ru^{V}=O center may accelerate proton-coupled electron transfer steps (Figure 1a).[37−41] This was initially accomplished by positioning three Ru(bda) centers around a water-filled pocket in macrocyclic architectures[37−39] and more recently advanced to the first macrocyclic mononuclear Ru(bda)-based catalyst equipped with a 2,2'-bipyridine (bpy) functionalized ligand opposite the metal center (Figure 1b).[40,41] The latter, while operating perfectly under acidic conditions with the sacrificial oxidant cerium(IV) ammonium nitrate (CAN) with high TOF of 140 s^{-1}, comparable to natural OEC-PSII, showed only very low TOF < 0.1 s^{-1} in photocatalytic studies with $[Ru(bpy)_3]^{2+}$ (bpy = 2,2′-bipyridine) as photosensitizer and $Na_2S_2O_8$ as sacrificial oxidant at neutral pH. Our detailed study[40] revealed the orientation of the Ru(bda) unit to be the reason which is only oriented in a favorable position for WNA under acidic conditions while under neutral conditions WNA is not observed, leading to a mechanistic switch to the slower bimolecular I2M pathway.

The aim of the current study is to explore the impact of the Ru(bda) orientation in macrocyclic mononuclear catalysts under neutral conditions on photocatalytic water oxidation. Toward this goal, three mononuclear Ru(bda) based catalysts (**1**-**3**) were synthesized bearing different heterocycles opposing the catalytic Ru^{V}=O center (Figure 1c). Detailed catalysis and H/D kinetic isotope effect (KIE) studies reveal that dibenzofuran catalyst **1**, similar to the previous 2,2'-bipyridine-based **M1** operates slowly via the I2M mechanism (TOF ∼ 0.01−0.12 s^{-1}) while both catalysts **2** (containing a dibenzothiophene group) and **3** (containing a carbazole group) operate via the WNA mechanism with significantly better performance (TOF = 0.5 s^{-1} and 0.22 s^{-1}, respectively). These results could be rationalized by detailed structural investigations including orientation angle-dependent energy profile diagrams for the three catalysts that show the advantageous orientation of the catalytic Ru^{V}=O center for catalysts **2** and **3**.

2. RESULTS AND DISCUSSION

Complexes **1**−**3** were obtained following a two-step synthetic procedure (Scheme 1). In the first step, the ditopic ligands (**8**−**10**) were synthesized via a palladium-catalyzed Suzuki-Miyaura cross-coupling reaction between the axial pyridine ligand 3-(4-(4,4,5,5-tetramethyl-1,3,2-dioxaborolan-2-yl)phenoxy)pyridine (**4**) and dibromo derivatives of various heterocycles (**5**−**7**). In the final step, complexes **1**-**3** were obtained following 2-fold ligand exchange of $[Ru(bda)(DMSO)_2]$ (DMSO = dimethyl

Scheme 1. Synthesis of the Mononuclear Ru(bda) Complexes 1−3

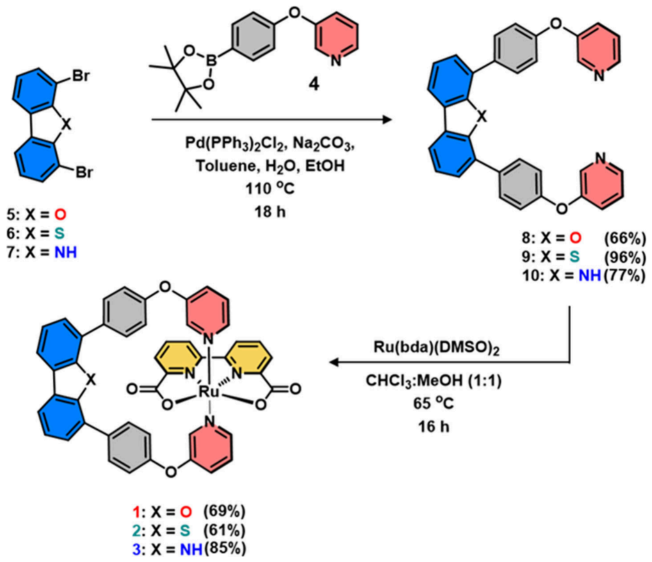

sulfoxide) with the respective bidentate ligands. All complexes contain a single Ru(bda) subunit as the active catalytic center with a surrounding heterocycle-containing moiety for the creation of a revolving macrocyclic structure. The target molecules were fully characterized by NMR spectroscopy, mass spectrometry and X-ray crystallography.

2.1. Single Crystal X-ray Analyses

First structural insights were obtained from single crystal X-ray analysis of the macrocycles grown from dichloromethane/methanol solutions. The ORTEP representations for the three crystal structures confirm the mononuclear and macrocyclic natures of the catalyst (Figure 2 and Tables S3−S6). The bridging macrocycles containing dibenzofuran or dibenzothiophene are found in front of the Ru^{II} center with obtuse O−Ru−O angles of 122.1° for both **1** and **2** that are comparable to reported acyclic mononuclear complexes such as $[Ru(bda)(pic)_2]$.[28] The Ru centers in **1** and **2** are six-coordinated with the N_{ax}-Ru-N_{ax} axes being slightly deviated from the ideal linear orientation with bond angles around 171.3° and 175.2° for **1** and **2**, respectively (Figure 2a,c), and torsional angles between 66.9 and 87.0° for the pyridine units (Figure 2b,d). In the case of macrocycle **1**, two methanol molecules bound to the bda equatorial ligand via hydrogen-bonding (distance of 2.03 Å) could be resolved within the solvent-filled pocket in front of the Ru center. For macrocycle **3**, the crystal structure revealed a different arrangement. Thus, while the first coordination sphere around the Ru^{II} center is inconspicuous with an O−Ru−O obtuse angle of 123° and the axial pyridine units oriented almost in a linear fashion with a N_{ax}-Ru-N_{ax} bond angle of 179.0°, a N−H····O hydrogen bond (2.03 Å) between a carboxylate of the equatorial bda ligand and the carbazole unit orients the Ru(bda) unit into a side-on arrangement to the macrocycle (Figure 2c,f).

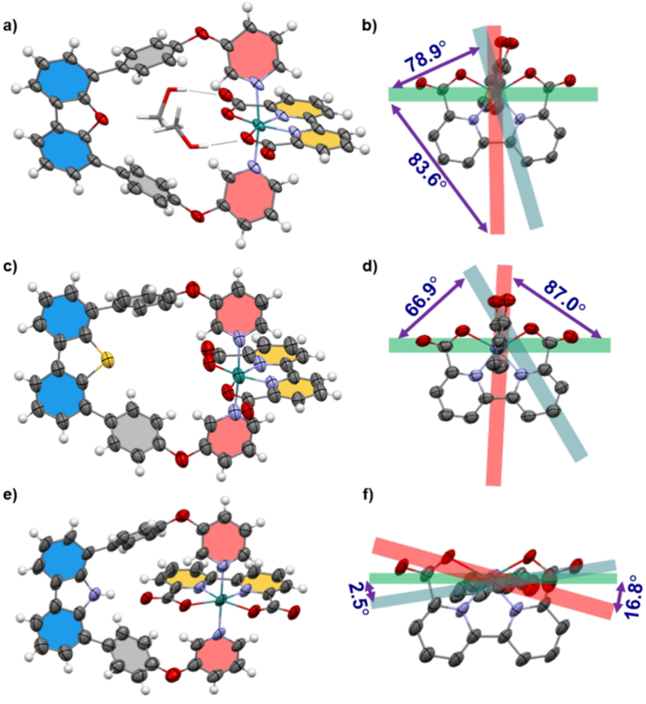

Figure 2. Single crystal X-ray structures of the catalysts (a) **1**, (c) **2**, and (e) **3**. ORTEP diagram with the thermal ellipsoids set at 50% probability: gray = C, white = H, red = O, blue = N, turquoise = Ru, yellow = S. Only those solvent molecules which are within the short contact (vdW distance) of the catalyst are shown. Some of the organic solvent molecules are omitted for clarity. Comparison of the X-ray crystal structures of (b) **1**, (d) **2**, and (f) **3** regarding the torsion angles of the axial pyridyl rings relative to the respective Ru center (plane generated by the atoms py(N_{ax})-C(=O)−Ru-C(=O)-py-(N_{ax})). From the axial ligands, only the coordinating pyridine moiety is shown for the sake of clarity (ORTEP diagram with thermal ellipsoids set at 50% probability; gray = C, white = H, red = O, blue = N, turquoise = Ru, yellow = S).

2.2. NMR Studies

^1H NMR spectra of mononuclear macrocycles **1**-**3** in a 5:1 CD_2Cl_2:CD_3OD mixture corroborate the results from single crystal analysis. As shown in Figures 3a and S4, macrocycle **1** exhibits significant line broadening at room temperature which, however, changes into a well-resolved pattern at 231 K where all the individual proton signals can be assigned based on one-dimensional (1D) and two-dimensional (2D) NMR spectroscopy techniques (Figures S5−S7). Nevertheless, this signal broadening suggests the presence of some conformational heterogeneity with an activation energy barrier of 77.2 kJ mol^{-1} being deducible from line shape analysis (Figure S8).[42] With only one set of signals for all chemically nonequivalent protons at 231 K for **1** and at 295 K for **2** the presence of highly symmetrical structures can be assumed. For both compounds, the chemical shifts of the axial pyridine protons *H*1 and *H*4 are the most characteristic. Based on the chemical shifts of the *ortho*-protons *H*1 and *H*4, the former being shielded by the aromatic ring current of the bipyridine ligand and the latter one being deshielded, the predominant conformations in solution for these complexes are in line with the crystallographic data discussed above (Figures 3b, c and S9, S10). In the case of macrocycle **3** containing carbazole the resonances for the *ortho*-*H*4 and *H*1 protons are shifted less pronounced than in **1** or **2**. This, together with the carbazole N*H* proton being observed at 10.7 ppm, indicating H-bonding with the bda carboxylate (Figure S31), corroborates the side-on orientation of the macrocycle **3** with regard to the Ru(bda) unit (Figures 3d and S11, S12).

2.3. Photocatalytic Water Oxidation

The performance as water oxidation catalysts was studied for all three macrocycles using a three-component system in 50 mM phosphate buffered CH_3CN/H_2O 4:6 at pH 7 with $[Ru(bpy)_3Cl_2]$ (c = 1.5 mM) as a photosensitizer and $Na_2S_2O_8$ (c = 37 mM) as a sacrificial electron acceptor under illumination with a Xenon lamp equipped with a solar filter at a power of 100 mW cm^{-2} (Figures 4 and S13−S18) and with the evolution of O_2 being detected with a Clark electrode. For **1** containing the dibenzofuran unit the initial O_2 evolution rate with respect to the catalyst concentration exhibited a second-order dependency with modest TOF values in the range of 0.01−0.12 s^{-1} (c = 0−20 μM) and a TON_{max} of 9 (Figures 4b and S13). Specifically, the fact that almost no oxygen is generated at low concentrations corroborates the prohibition of the WNA pathway, leading to the onset of oxygen evolution only at higher concentrations via the bimolecular I2M pathway. Likewise in D_2O/CH_3CN, a quadratic rate dependence is observed, albeit the kinetic isotope effect (KIE) of 1.5 is at the upper limit for an I2M mechanism. This might be attributed to the rate-determining step being shifted to the preceding proton-coupled oxidation from Ru^{IV}−OH to Ru^{V}=O at higher concentrations where the bimolecular coupling becomes fast (Figure S14). Remarkably,

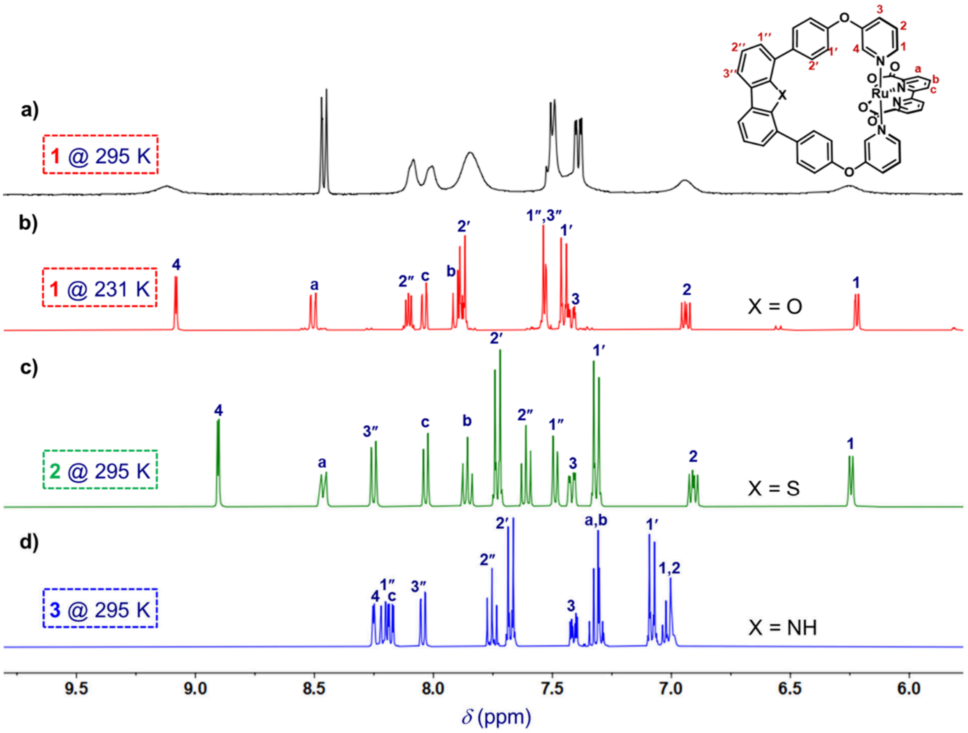

Figure 3. Aromatic region of the ^{1}H NMR spectra (400 MHz, CD_2Cl_2:CD_3OD (5:1)) of the Ru(bda) complexes (a) **1**, (c) **2**, and (d) **3** at 295 K and of (b) **1** at 231 K. Numbered signals correspond to protons labeled in the structure.

the structurally similar benzothiophene congener **2** behaved entirely different, exhibiting a linear dependency between initial O_2 evolution rate and catalyst concentration and significantly higher TOF of 0.5 s^{-1} and TON_{max} of 27 (Figure 4b and S15, S16). The same linear dependency in deuterated water indicates a mechanistic switch to WNA for **2** (Figure S16). In the case of carbazole macrocycle **3**, an intermediate performance with TOF of 0.22 s^{-1} and TON_{max} of 25 is observed and based on linear relationships between catalyst concentration and rate, also here a unimolecular WNA mechanism can be assumed (Figure 4b and S17, S18).

2.4. Mechanistic Explanations

The results obtained from our photocatalytic studies, in particular with regard to the mechanistic switch from slow I2M for **1** toward faster WNA for **2** cannot be explained by the structural insights obtained by single crystal X-ray analysis and NMR studies on the precursor Ru^{II} complexes where both compounds showed very similar structures. Accordingly, we hypothesized that different conformations might prevail for the macrocycles in their catalytically active $Ru^V{=}O$ state in the aqueous environment (Figure 5). To this end, DFT calculations were carried out with implicit consideration of the solvent within the Conductor-like Polarizable Continuum Model (CPCM) for the macrocycles bearing $Ru^V{=}O$ metal-oxo species for a better understanding of the relationship between the observed mechanisms and the orientation of the recognition site relative to the catalytic center.[40,43]

First, we optimized the structures at the two most extreme conformations of the bda ligand, namely, 0 and 180° (Figure 5a). Upon optimization of the 0° starting geometry, all three molecules converged to an energetically more favorable side-on conformation, corresponding to an orientation angle of 58°. For the 180° end point, catalyst **1** remained in this extreme position, whereas catalysts **2** and **3** adopted orientations of 167° and 175°, respectively (Figure 5b-d). After establishing the two end point conformations, the intermediate structures were generated for all catalysts by detailed theoretical calculations, the nudged elastic band (NEB) method. NEB calculations have been performed by employing the BP86 (Figure 5) and B3LYP[44−46] (Figure S19) functionals showing similar results. More details are given in the Computational Method section. Following this approach, we created an orientation angle (θ)-dependent energy profile exhibiting the energetically favorable conformations (local minima) and the electronic energy barriers associated with the rotational movement of the equatorial bda ligand.

For catalyst **1**, among three conformations of low energy, conformation (v) in Figure 5b, in which the Ru center points outward from the cavity while the bda unit is rotated inward, is the most energetically favored, with electronic energies 35.7 and 41.5 kJ mol^{-1} lower than those of conformations (i) and (iii), respectively. Taking this conformation as the prevalent one in the $Ru^V{=}O$ state, it can explain why this catalyst cannot take advantage of proton-coupled electron transfer steps in a water-filled pocket and in addition suffers like our earlier catalyst (Figure 1b) from sterical constraints originating from the orientation of the axial pyridine units, which even slow down the alternative bimolecular I2M pathway. The rationale behind the conformational switch is in our opinion not due to the additional steric demand of the protruding oxygen at the Ru center but due to the hydrophobic effect in water, which favors the uptake of the aromatic bda unit within the aromatic pocket of the macrocycle by π-π stacking to the phenoxy linkers (Figure 6a and Supplementary Video S1).

For catalyst **2** likewise three local minima could be identified by our calculations, corresponding to the conformers (i), (iii) and (v) (Figure 5c). However, here the energetics are different, and all three conformations might coexist. As shown in Figure

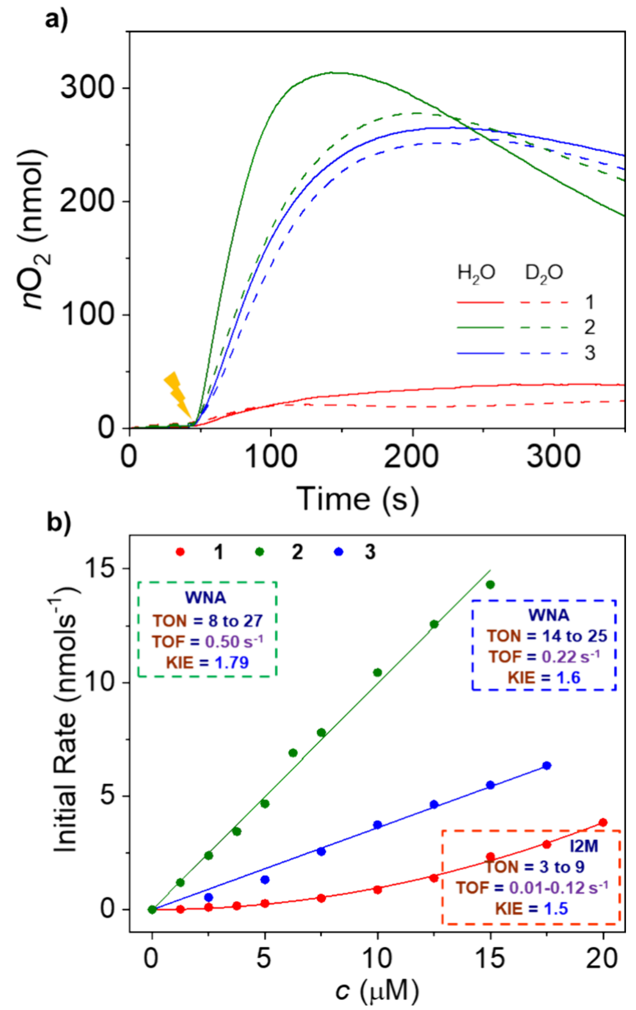

Figure 4. Photocatalytic water oxidation experiments (c = 25 μM, taken for comparison) with catalysts **1** (red), **2** (green) and **3** (blue) in water/acetonitrile 6/4 composition (pH 7, 50 mM phosphate buffer), c(PS, $Ru(bpy)_3Cl_2$) = 1.5 mM, $c(Na_2S_2O_8)$ = 37 mM. (a) Detection of oxygen generated over time. The lighting symbol indicates the start of sample irradiation at t = 40 s. (b) Plot of the initial rates (obtained by linear fit of O_2 evolution curves) of O_2 evolution against the catalyst amount for catalysts **1** (red), **2** (green) and **3** (blue) in water/acetonitrile 6/4 composition (pH 7, 50 mM phosphate buffer) with quadratic/linear regression.

6b, attractive and repulsive noncovalent chalcogen interactions are clearly identified: an attractive one in conformer (i) between the sulfur atom of the thiophene unit and a carbonyl oxygen of the bda ligand (distance ∼ 2.8 Å) and a repulsive one in conformer (iii) between the sulfur atom and an H−C group from the bda ligand (distance ∼ 2.1 Å). These interactions support conformations (i) and (iii) which are more favorable for both WNA and I2M mechanisms, with the former one prevailing in our experiments according to our kinetic analysis. It is noteworthy to comment that a significantly high rotational energy barrier of 117.7 kJ mol^{-1} originates between conformations (iii) and (v) due to sterical encumbrance upon passage of the bda ligand around the larger sulfur of the dibenzothiophene unit (Figures 5c, 6b and Supplementary Video S2). Accordingly, this transition state might not be traversable under our experimental conditions, and a fraction of the molecules might be trapped in conformation (v) where they do not contribute significantly to water oxidation with a performance similar to the one observed for the dibenzofuran derivative following the I2M pathway.

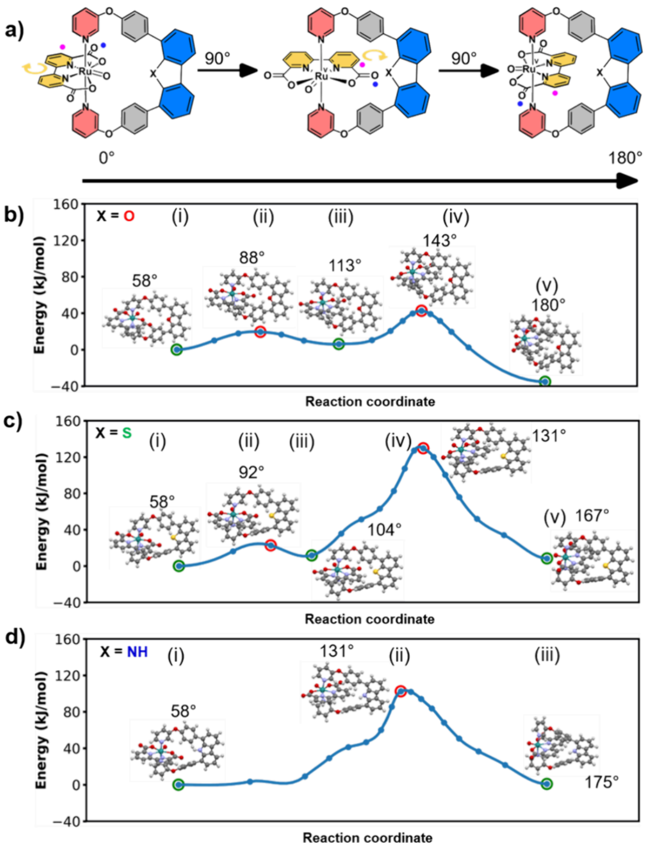

Figure 5. (a) Rotation of the equatorial bda ligand in the Ru(V) state from outside the recognition site (58°) to fully inside (180°, 167°, 175°) and corresponding orientation angle (θ) dependent energy diagrams for (b) **1**, (c) **2** and (d) **3**. θ has been varied to different extents to exhibit the energetically preferred conformation and the required energy barrier for rotation of the coordination sphere. The molecular structures are rendered with the Open Visualization Tool (OVITO) software.[47] Selected conformations are depicted alongside. The H, C, N, O, S, and Ru atoms are marked with white, gray, blue, red, yellow, and sand green, respectively.

Finally, for **3** both the starting and end point conformations (i) and (iii) remain at the lowest energy level with a negligible energy difference of 0.96 kJ mol^{-1} (Figure 5d). Thus, both species may coexist, and for the same arguments as discussed above we may assume that the observed rates for oxygen generation are attributable to those molecules prevailing in conformation (i), which affords a water-filled cleft in front of the $Ru^V{=}O$ center that is considered favorable for the WNA pathway. Also here, the rotational energy barrier for the interconversion between (i) and (iii) is found to be rather high with a value of around 102.3 kJ mol^{-1} (Figure 6c). Like in the former case, this high barrier originates from steric encumbrance as the carbazole NH has to distort significantly to enable the passage of the bda unit during the rotational process from conformer (i) to conformer (iii) (Figure 5d and Supplementary Video S3).

3. CONCLUSIONS

In summary, inspired by enzymatic clefts with their exceptional second coordination sphere effects, Ru(bda) water oxidation

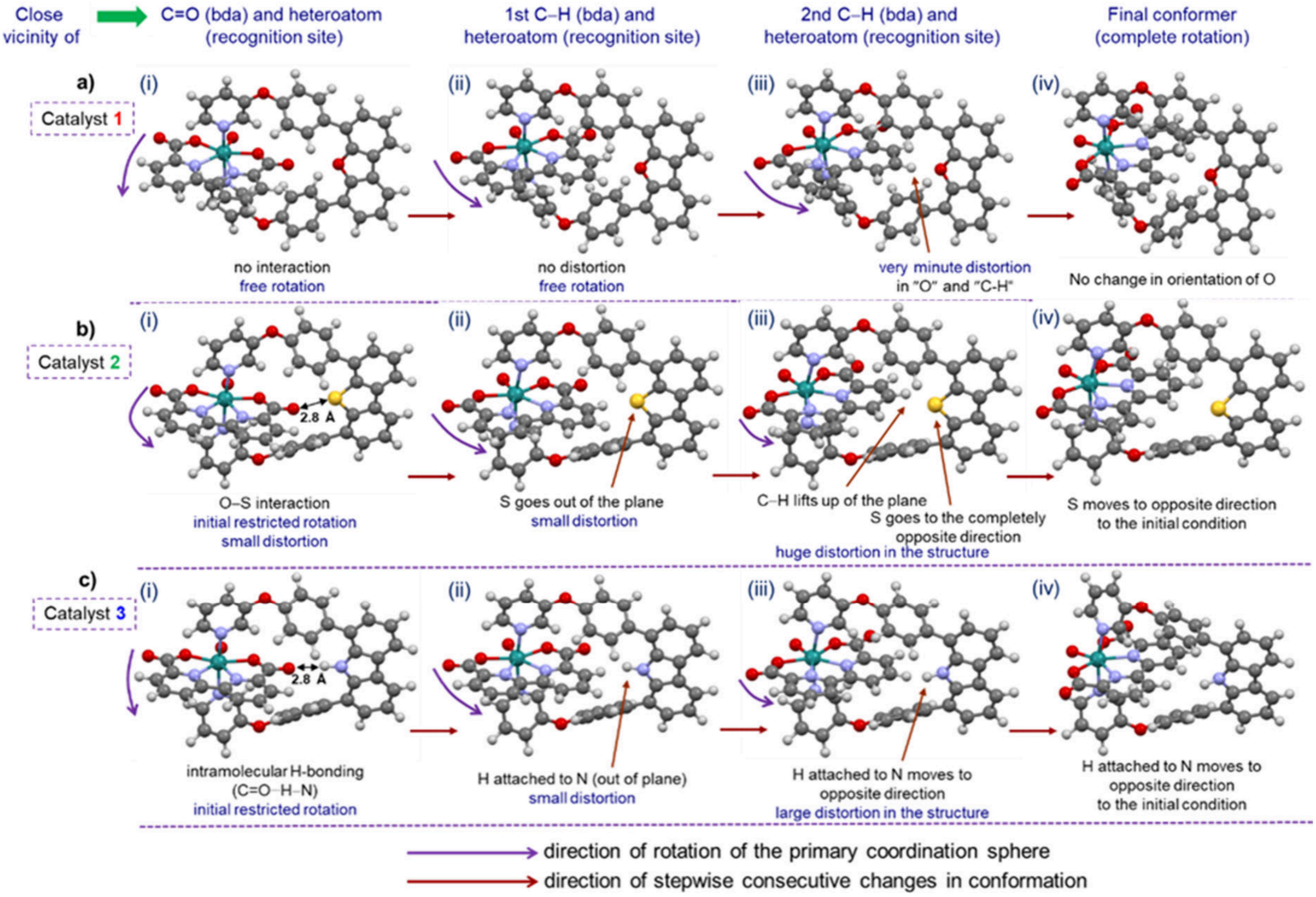

Figure 6. Illustration of the stepwise conformational changes of the catalysts (a) **1**, (b) **2** and (c) **3** during the gradual rotation of the primary coordination sphere (indicated by violet arrows). The scheme demonstrates the reason behind the difference in the energy barrier for all of the catalysts.

catalysts were embedded in three different macrocycles to study the impact of conformational preferences on the photocatalytic water oxidation performance. Depending on the preferential orientation of the macrocycle, different pathways for water oxidation were observed. Thus, dibenzofuran-based macrocycle **1** is trapped in a conformation that does not support the unimolecular WNA pathway and therefore lags behind the other two macrocycles with regard to its catalytic activity. In contrast, noncovalent interactions between NH and S atoms of the other two macrocycles (carbazole, dibenzothiophene) and oxygen atoms of the equatorial bda ligand stabilize a more favorable conformation for the WNA pathway. Among the three catalysts, dibenzothiophene-based **2** is found to be the best performing one, exhibiting a TOF of 0.5 s^{-1} and TON_{max} of 27. With these results, our study contributes to a better understanding of second coordination sphere engineering for Ru(bda)-based water oxidation catalysts. Our approach for the creation of cleft-like structures by rotational restriction of macrocyclic units surrounding a transition metal center might ultimately afford tailored nanoenvironments that organize substrate molecules for desired catalytic transformations as commonly observed in natural enzymes. Toward this goal, a significant challenge is to keep control of the prevailing conformations that are distinct for the different Ru oxidation states as illustrated by our in-depth NMR studies, crystal structure analysis, and theoretical calculations.

4. METHODS

4.1. Synthesis of Bidentate Ligands

1,8-Bis(4-(pyridin-3-yloxy)phenyl)dibenzo[b,d]furan (8). A mixture of 4,6-dibromodibenzo[b,d]furan (**5**) (100 mg, 307 μmol, 1.0 equiv), 3-(4-(4,4,5,5-tetramethyl-1,3,2-dioxaborolan-2-yl)phenoxy)-pyridine (**4**) (210 mg, 706 μmol, 2.3 equiv) and 2 M Na_2CO_3 aqueous solution (1.25 mL, 2.5 mmol, 8.0 equiv) in toluene (2.5 mL) and ethanol (0.6 mL) was degassed under nitrogen following three consecutive alternate vacuum-nitrogen cycles. Subsequently, $PdCl_2(PPh_3)_2$ (22 mg, 30.7 μmol, 0.1 equiv) was added, and the resulting mixture was heated at 110 °C for 18 h. After cooling down to room temperature, the solvent was removed under reduced pressure and the residue was diluted with dichloromethane (15 mL). The organic phase was separated, and the aqueous phase extracted with dichloromethane (3 × 25 mL). The combined organic phases were dried over anhydrous Na_2SO_4 and concentrated under reduced pressure. The residue was purified by flash chromatography (SiO_2, dichloromethane/ethyl acetate 75/25 to 70/30) to yield ligand **8** (103 mg, 203 μmol, 66%) as a colorless solid. **^{1}H NMR** (400 MHz, $CDCl_3$, rt): δ [ppm] = 8.50 (d, $^4J_{H-H}$ = 2.6 Hz, 2H, *H4*), 8.40 (dd, $^3J_{H-H}$ = 4.5 Hz, $^4J_{H-H}$ = 0.9 Hz, 2H, *H1*), 7.98 − 7.94 (m, 6H, *H2′* and *H1″/H3″*), 7.64 (dd, $^3J_{H-H}$ = 7.6 Hz, $^4J_{H-H}$ = 1.0 Hz, 2H, *H3″/H1″*), 7.46 (t, $^3J_{H-H}$ = 7.6 Hz, 2H, *H2″*), 7.38 (ddd, $^3J_{H-H}$ = 8.4 Hz, $^4J_{H-H}$ = 2.8, 1.3 Hz, 2H, *H3*), 7.29 (dd, $^3J_{H-H}$ = 8.3, 4.6 Hz, 2H, *H2*), 7.17 − 7.14 (m, 4H, *H1′*). **^{13}C NMR** (100 MHz, $CDCl_3$, rt): δ (ppm) = 156.2, 153.7, 153.1, 144.7, 141.7, 132.1, 130.2, 126.5, 125.7, 125.0, 124.7, 124.2, 123.5, 119.8, 118.9. **HRMS** (**ESI-TOF**, pos. mode, MeCN:$CHCl_3$ 1:1): *m/z* calcd for $C_{34}H_{22}N_2O_3$+Na^+: 529.1630 [*M* +Na]$^+$; found: 529.1506.

1,8-Bis(4-(pyridin-3-yloxy)phenyl)dibenzo[b,d]thiophene (9). A mixture of 4,6-dibromodibenzo[b,d]thiophene (**6**) (150 mg, 439 μmol, 1.0 equiv), 3-(4-(4,4,5,5-tetramethyl-1,3,2-dioxaborolan-2-yl)phenoxy)pyridine (**4**) (299 mg, 964 μmol, 2.2 equiv) and 2 M Na_2CO_3 aqueous solution (1.8 mL, 3.5 mmol, 8.0 equiv) in toluene (3.8 mL) and ethanol (1.0 mL) was degassed under nitrogen following three consecutive alternate vacuum-nitrogen cycles. Subsequently, $PdCl_2(PPh_3)_2$ (31 mg, 44 μmol, 0.1 equiv) was added, and the resulting mixture was heated at 110 °C for 18 h. After cooling down to room temperature, the solvent was removed under reduced pressure and the residue was diluted with dichloromethane (15 mL). The organic phase was separated, and the aqueous phase extracted with dichloromethane (3 × 25 mL). The combined organic phases were dried over anhydrous Na_2SO_4 and concentrated under reduced pressure. The residue was purified by flash chromatography (SiO_2, dichloromethane/ethyl acetate 80/20) to yield ligand **9** (220 mg, 421 μmol, 96%) as a pale pink solid. **^{1}H NMR** (400 MHz, $CDCl_3$, rt): δ [ppm] = 8.49 (d, $^4J_{H-H}$ = 2.5 Hz, 2H, *H4*), 8.42 (dd, $^3J_{H-H}$ = 4.4 Hz, 2H, *H1*), 8.20 (d, $^3J_{H-H}$ = 7.8 Hz, 2H, *H1″/H3″*), 7.71 (d, 4H, $^3J_{H-H}$ = 8.5 Hz, *H2′*), 7.58 (t, $^3J_{H-H}$ = 7.6 Hz, 2H, *H2″*), 7.48 (dd, $^3J_{H-H}$ = 7.4 Hz, 2H, *H3″/H1″*), 7.42 (ddd (broad), $^3J_{H-H}$ = 8.5 Hz, 2H, *H3*), 7.32 (dd, $^3J_{H-H}$ = 8.3, 4.6 Hz, 2H, *H2*), 7.14 (d, $^3J_{H-H}$ = 8.5 Hz, 4H, *H1′*). **^{13}C NMR** (100 MHz, $CDCl_3$, rt): δ (ppm) = 156.4, 153.5, 144.8, 141.9, 138.5, 136.6, 136.2, 136.1, 130.0, 127.1, 126.1, 125.3. 124.2, 120.7, 118.9. **HRMS** (**ESI-TOF**, pos. mode, MeCN:$CHCl_3$ 1:1): *m/z* calcd for $C_{34}H_{22}N_2O_2S+H^+$: 523.1402 [*M*+H]$^+$; found: 523.1483.

1,8-Bis(4-(pyridin-3-yloxy)phenyl)-9*H*-carbazole (10). A mixture of 1,8-dibromo-9*H*-carbazole (**7**) (200 mg, 615 μmol, 1.0 equiv), 3-(4-(4,4,5,5-tetramethyl-1,3,2-dioxaborolan-2-yl)phenoxy)pyridine (**4**) (402 mg, 1.35 mmol, 2.2 equiv) and 2 M Na_2CO_3 aqueous solution (2.8 mL, 4.9 mmol, 8.0 equiv) in toluene (5.2 mL) and ethanol (1.3 mL) was degassed under nitrogen following three consecutive alternate vacuum-nitrogen cycles. Subsequently, $PdCl_2(PPh_3)_2$ (43 mg, 62 μmol, 0.1 equiv) was added, and the resulting mixture was heated at 110 °C for 18 h. After cooling down to room temperature, the solvent was removed under reduced pressure and the residue was diluted with dichloromethane (15 mL). The organic phase was separated, and the aqueous phase extracted with dichloromethane (3 × 25 mL). The combined organic phases were dried over anhydrous Na_2SO_4 and concentrated under reduced pressure. The residue was purified by flash chromatography (SiO_2, dichloromethane/ethyl acetate 70/30 to 65/35) to yield ligand **10** (238 mg, 471 μmol, 77%) as a brown solid. **^{1}H NMR** (400 MHz, $CDCl_3$, rt): δ [ppm] = 8.53 (s, 1H, -N*H*), 8.49 (d, $^4J_{H-H}$ = 2.6 Hz, 2H, *H4*), 8.41 (dd, $^3J_{H-H}$ = 4.6 Hz, $^4J_{H-H}$ = 1.4 Hz, 2H, *H1*), 8.11 (dd, 2H, $^3J_{H-H}$ = 7.2 Hz, *H1″/H3″*), 7.67 − 7.64 (m, 4H, *H2′*), 7.43 (dd, $^3J_{H-H}$ = 7.4 Hz, $^4J_{H-H}$ = 1.2 Hz, 2H, *H3″/H1″*), 7.39 (ddd, $^3J_{H-H}$ = 8.4 Hz, $^4J_{H-H}$ = 2.8, 1.4 Hz, 2H, *H3*), 7.35 (t, $^3J_{H-H}$ = 7.6 Hz, 2H, *H2″*), 7.30 (dd, $^3J_{H-H}$ = 8.4, 4.6 Hz, $^5J_{H-H}$ = 0.6 Hz, 2H, *H2*), 7.18 − 7.14 (m, 4H, *H1′*). **^{13}C NMR** (100 MHz, $CDCl_3$, rt): δ (ppm) = 156.2, 153.5, 144.9, 141.8, 137.1, 134.7, 130.0, 126.0, 125.9, 124.2, 124.1, 124.0, 120.3, 119.7, 119.4. **HRMS** (**ESI-TOF**, pos. mode, MeCN:$CHCl_3$ 1:1): *m/z* calcd for $C_{34}H_{23}N_3O_2+H^+$: 506.1790 [*M*+H]$^+$; found: 506.2756.

4.2. Synthesis of the Mononuclear Catalysts

[Ru(bda)1,8-bis(4-(pyridin-3-yloxy)phenyl)dibenzo[b,d]-furan] (1). [Ru(bda)$(DMSO)_2$] (134 mg, 261 μmol, 1.1 equiv) and ligand **8** (118 mg, 237 μmol, 1.0 equiv) were dissolved in a degassed mixture of chloroform (40 mL) and methanol (40 mL) and stirred for 16 h at 65 °C under nitrogen atmosphere. After the mixture was cooled to room temperature and the completion of the reaction using TLC confirmed, the solvent was removed under reduced pressure. The residue was purified by column chromatography (SiO_2, dichloromethane/methanol = 93/7) and isolated as the first fraction to yield complex **1** (138 mg, 162 μmol, 69%) as a dark red solid. **^{1}H NMR** (400 MHz, CD_2Cl_2:CD_3OD (5:1), 231 K): δ [ppm] = 9.08 (d, $^4J_{H-H}$ = 2.7 Hz, 2H, *H4*), 8.51 (dd, $^3J_{H-H}$ = 8.2 Hz, $^4J_{H-H}$ = 1.2 Hz, 2H, *Ha*), 8.11 (t, $^3J_{H-H}$ = 8.8 Hz, 2H, *H2″*), 8.03 (dd, $^3J_{H-H}$ = 7.7 Hz, $^4J_{H-H}$ = 1.1 Hz, 2H, *Hc*), 7.94 − 7.84 (m, 6H, *Hb* and *H2′*), 7.56 − 7.50 (m, 4H, *H1″* and *H3″*), 7.47 − 7.44 (m, 4H, *H1′*), 7.42 (ddd, $^3J_{H-H}$ = 8.4 Hz, $^4J_{H-H}$ = 2.6, 1.1 Hz, 2H, *H3*), 6.95 (dd, $^3J_{H-H}$ = 8.4 Hz, $^4J_{H-H}$ = 5.4 Hz, 2H, *H2*), 6.22 (dd, $^3J_{H-H}$ = 5.5 Hz, $^4J_{H-H}$ = 1.2 Hz, 2H, *H1*). **^{13}C NMR** (100 MHz, CD_2Cl_2:CD_3OD (5:1), 231 K): δ (ppm) = 174.0, 159.4, 156.1, 153.6, 153.1, 152.7, 143.4, 142.7, 133.9, 132.0, 130.8, 128.9, 127.4, 126.1, 126.0, 125.6, 125.0, 123.5, 119.9, 118.9. **UV/vis** (CH_3CN/H_2O 4:6 (@ pH 7)): λ_{max} (ε) = 254 (42283), 302 (39153), 345 (18765), 454 (4954), 482 nm (4766 M-1 cm-1);**HRMS** (**ESI-TOF**, pos. mode, MeOH: dichloromethane 1:1): *m/z* calcd for $C_{46}H_{28}N_4O_7Ru+Na^+$: 873.1001 [*M*+Na]$^+$; found: 873.5352. **m.p.** > 300 °C.

[Ru(bda)1,8-bis(4-(pyridin-3-yloxy)phenyl)dibenzo[b,d]-thiophene] (2). [Ru(bda)$(DMSO)_2$] (240 mg, 463 μmol, 1.1 equiv) and ligand **9** (220 mg, 421 μmol, 1.0 equiv) were dissolved in a degassed mixture of chloroform (70 mL) and methanol (70 mL) and stirred for 14 h at 65 °C under nitrogen atmosphere. After cooling to room temperature and confirming the completion of the reaction using TLC, the solvent was removed under reduced pressure. The residue was purified by column chromatography (SiO_2, dichloromethane/methanol = 93/7) and isolated as the first fraction to yield complex **2** (221 mg, 255 μmol, 61%) as a dark red solid. **^{1}H NMR** (400 MHz, CD_2Cl_2:CD_3OD (5:1), rt): δ [ppm] = 8.90 (dd, $^4J_{H-H}$ = 2.6 Hz, 2H, *H4*), 8.46 (dq, $^3J_{H-H}$ = 8.2 Hz, $^4J_{H-H}$ = 1.5 Hz, 2H, *Ha*), 8.25 (dd, $^3J_{H-H}$ = 8.0 Hz, $^4J_{H-H}$ = 1.1 Hz, 2H, *H3″*), 8.03 (dd, $^3J_{H-H}$ = 7.7 Hz, $^4J_{H-H}$ = 1.1 Hz, 2H, *Hc*), 7.86 (t, $^3J_{H-H}$ = 7.9 Hz, 2H, *Hb*), 7.75 − 7.71 (m, 4H, *H2′*), 7.61 (t, $^3J_{H-H}$ = 7.6 Hz, 2H, *H2″*), 7.49 (dd, $^3J_{H-H}$ = 7.3 Hz, $^4J_{H-H}$ = 1.1 Hz, 2H, *H1″*), 7.42 (ddd, $^3J_{H-H}$ = 8.4 Hz, $^4J_{H-H}$ = 2.6, 1.1 Hz, 2H, *H3*), 7.33 − 7.30 (m, 4H, *H1′*), 6.91 (dd, $^3J_{H-H}$ = 8.4 Hz, $^4J_{H-H}$ = 5.6 Hz, 2H, *H2*), 6.25 (dd, $^3J_{H-H}$ = 5.5 Hz, $^4J_{H-H}$ = 0.6 Hz, 2H, *H1*). **^{13}C NMR** (100 MHz, CD_2Cl_2:CD_3OD (5:1), rt): δ (ppm) = 173.5, 159.6, 156.9, 154.6, 153.3, 144.1, 143.6, 139.7, 137.1, 136.4, 136.3, 131.9, 130.4, 128.0, 126.1, 125.9, 125.8, 125.1, 124.6, 120.8, 118.5. **HRMS** (**ESI-TOF,** pos. mode, MeOH:dichloromethane 1:1): *m/z* calcd for $C_{46}H_{28}N_4O_6RuS+Na^+$: 889.0773 [*M*+Na]$^+$; found: 889.5186. **m.p.** > 300 °C.

[Ru(bda)1,8-bis(4-(pyridin-3-yloxy)phenyl)-9*H*-carbazole] (3). [Ru(bda)$(DMSO)_2$] (113 mg, 229 μmol, 1.1 equiv) and ligand **10** (101 mg, 207 μmol, 1.0 equiv) were dissolved in a degassed mixture of chloroform (35 mL) and methanol (35 mL) and stirred for 16 h at 65 °C under nitrogen atmosphere. After cooling to room temperature and confirming the completion of the reaction using TLC, the solvent was removed under reduced pressure. The residue was purified by column chromatography (SiO_2, dichloromethane/methanol = 95/5) and isolated as the first fraction to yield complex **3** (144 mg, 169 μmol, 85%) as a dark red solid. **^{1}H NMR** (400 MHz, CD_2Cl_2:CD_3OD (5:1), rt): δ [ppm] = 10.7 (s, 1H, -N*H*), 8.25 (dd, $^4J_{H-H}$ = 2.5 Hz, 2H, *H4*), 8.21 (dd, $^3J_{H-H}$ = 8.1 Hz, $^4J_{H-H}$ = 1.0 Hz, 2H, *Ha/Hc*), 8.18 (dd, $^3J_{H-H}$ = 7.1 Hz, $^4J_{H-H}$ = 1.9 Hz, 2H, *H3″*), 8.04 (dd, $^3J_{H-H}$ = 7.8 Hz, $^4J_{H-H}$ = 1.0 Hz, 2H, *Hc/Ha*), 7.75 (t, $^3J_{H-H}$ = 7.8 Hz, 2H, *Hb*), 7.69 − 7.66 (m, 4H, *H2′*), 7.41 (ddd, $^3J_{H-H}$ = 7.8 Hz, $^4J_{H-H}$ = 2.7, 1.8 Hz, 2H, *H3*), 7.34 − 7.28 (m, 4H, *H1″* and *H2″*), 7.09 − 7.06 (m, 4H, *H1′*), 7.04 − 6.99 (m, 4H, *H1* and *H2*). **^{13}C NMR** (100 MHz, CD_2Cl_2:CD_3OD (5:1), rt): δ (ppm) = 173.0, 160.1, 157.1, 154.5, 153.8, 144.3, 141.7, 137.9, 136.9, 131.9, 131.3, 127.4, 126.8, 126.5, 125.6, 125.4, 123.9, 123.8, 119.5, 119.2, 119.1. **HRMS** (**ESI-TOF**, pos. mode, MeOH:dichloromethane 1:1): *m/z* calcd for $C_{46}H_{29}N_5O_6Ru+Na^+$: 872.1161 [*M*+Na]$^+$; found: 872.5496. **m. p.** > 300 °C.

4.3. Single Crystal X-ray Analysis

Single crystals of the pocket shaped Ru(bda) based catalysts (**1**-**3**) are grown at neutral conditions where Ru is in the initial Ru^{II} state. For crystallization, diethyl ether or *n*-hexane is allowed to diffuse into a dichloromethane:methanol (1:1) solution of the individual compounds (*c* = 1.0 mg in 1.0 mL). All of the samples are stored in a refrigerator at 5 °C for crystallization. Single crystal X-ray diffraction data for **1**-**3** were collected at the P11 beamline at DESY. The diffraction data were collected by a single 360° φ scan at 100 K. The diffraction data were indexed, integrated, and scaled using the XDS program package.[48] The structures were solved using SHELXT,[49] expanded with Fourier techniques and refined using the SHELXL software package.[50] Hydrogen atoms were assigned at idealized positions and were included in the calculation of structure factors. All non-hydrogen atoms in the main residue were refined anisotropically. Heavily disordered solvent molecules that cannot be modeled satisfactorily were treated by the SQUEEZE[51] routine implemented in the program package PLATON.[52] Other disordered solvent molecules and disordered parts in the main residue were modeled with constraints and restraints using standard SHELX commands SAME, RIGU, DELU, SADI, and ISOR. The diffraction data for **2** was analyzed as twins using HKLF5 data generated by the TwinRotMat function implemented in PLATON.[52] For the crystal structure of **1**, several level A alerts were found by the checkcif routine[53] implemented in PLATON.[52] These alerts indicate residual density around the Ru center, which may be caused by the absence of absorption correction due to the single axis goniometer at P11.

4.4. Photocatalytic Water Oxidation

Photocatalytic water oxidation experiments were carried out at 20 °C following a standardized procedure from our previous publications.[39,54−56] In order to detect oxygen, an Oxygraph Plus Clark-electrode system with a transparent and temperature-controlled reaction chamber (Hansatech Instruments Ltd.) was used. Sample irradiation was achieved by a complete plug-and-play light source system including a 150 W xenon arc lamp (Newport) equipped with a cutoff filter (400 nm, Thorlabs). Prior to the measurement, the power of the sun simulation was calibrated to an intensity of 100 mW cm^{-1} applying a collinear light path with collimated light. The calibration was performed with a PM 200 optical power meter equipped with a S121C sensor (Thorlabs), which was installed in a modified oxygen chamber (Hansatech Instruments Ltd.) combined with a CCS 200/M wide range spectrometer (Thorlabs). All of the experiments were conducted under the same operation conditions (V = 2 mL, T = 20 °C, stirring speed = 100 rpm). Following a standard procedure, a stock solution of photosensitizer (PS) $[Ru(bpy)_3]Cl_2$ and $Na_2S_2O_8$ as a sacrificial electron acceptor (SEA) in 4:6 $CH_3CN:H_2O$ composition (pH 7, 50 mM phosphate buffer) was prepared in the dark ($c(Na_2S_2O_8)$ = 37 mM, $c([Ru(bpy)_3]Cl_2)$ = 1.5 mM) before each experiment. Then, an aliquot of this solution (1.5 mL) was transferred to the reaction chamber and mixed with varying amount of catalyst concentration (0.5 mL) in the dark. Irradiation of the sample was started after the baseline was constant (~40 s) to allow thermal equilibration of the sample at the same temperature. For the evaluation of the data, a blank measurement in absence of catalyst was subtracted from each measurement of concentration-dependent experiments. To benchmark the novel catalysts, the respective turnover frequency (TOF) and turnover number (TON) were determined. The TON, which is defined as total amount of evolved oxygen divided by the amount of used catalyst, is calculated for each concentration and the highest TON is reported. The TOF for each concentration can be determined by linear regression fit of the first 5−10 s of catalysis from the plot of evolved oxygen versus reaction time. The extracted value represents the initial rate of catalysis for the respective concentration. The averaged TOF was then determined from the slope of a linear regression of the initial rates of each concentration versus the respective catalyst amount. In the case of a quadratic dependency, a range of the observed TOF values, calculated for each concentration, is given.

4.5. Kinetic Isotope Experiments

Following the standard procedures established in our laboratory,[39,55,56] the experiments were performed using a Oxygraph Plus Clark-electrode system (Hansatech Instruments Ltd.) for oxygen detection (T = 20 °C, stirring speed = 100 rpm). If the relative reaction rates for nondeuterated and deuterated solvent differ by approximately a factor of 2, the reaction is characterized by a primary deuterium kinetic isotope effect (KIE) and a direct O−H/D bond cleavage is involved in the rate-determining step of the WNA pathway.[57] By contrast, for the bimolecular I2M mechanism, no direct hydrogen substitution takes place and thus a secondary kinetic isotope effect (KIE = 0.7−1.5) is observed.[57] The experiments under photocatalytic conditions were performed in accordance with the procedures described for photocatalytic water oxidation. Therefore, a stock solution of photosensitizer ($c([Ru(bpy)_3]Cl_2)$ = 1.5 mM) and the SEA ($c(Na_2S_2O_8)$ = 37 mM) in 4:6 $CH_3CN:H_2O$ composition (H_2O or D_2O (99.9% purity); pH 7, 50 mM phosphate buffer) was prepared in the dark. An aliquot of this solution (1.5 mL) was then mixed with varying catalyst concentration (total volume: 2 mL) in the dark. Irradiation was started at 40 s to allow thermal equilibration of the sample at a constant temperature of 20 °C. The reaction rate constants in H_2O ($k(H_2O)$) and D_2O ($k(D_2O)$) were calculated by determining the initial rate of catalysis for each concentration (linear regression of the oxygen evolution curve during the first five to ten seconds of the reaction).

4.6. Computational Methods

To evaluate the energy of **1**-**3** evolving according to the orientation of the bda group with respect to the Ru catalytic center, nudged elastic band (NEB) calculations using Kohn−Sham density functional theory were carried out. First, we built and geometry-optimized the 0° and 180° conformers of catalyst **1**−**3** (Figure 5a). After optimization, the 0° conformers relaxed to ~58° for all three catalysts **1**−**3** (Figure 5b−d), indicating that ~58° is the preferred angle. The 180° conformers converged to 180°, 167°, and 175° for catalysts **1**−**3**, respectively. These optimized geometries were then used as the initial and final images in the NEB calculations. The $Ru^V{=}O$ states are modeled to check the key O−O formation step. The results for catalysts **1**-**3** in the $Ru^V{=}O$ state are shown in Figure 5b−d.

The angle dependent electronic energy profile was calculated with climbing image nudged elastic band (CI-NEB) method as implemented in ORCA 5.0.4 software.[58−61] The Becke-Perdew (BP86) functional and Grimme D3 dispersion corrections,[62,63] and Triple-Zeta Valence Polarization (def2-TZVP) basis set were used.[64] Selected structures were also recomputed with the B3LYP functional.[65−67] Similar NEB results have also been obtained with the B3LYP functional. The Conductor-like Polarizable Continuum Model (CPCM) implicit solvent for water was used to approximately include the effect from the solvent.[68] The TightScf keyword was used for the SCF setup.

Low spin state is employed in the calculation, which is generally recognized for Ru(bda) structures.[68−71] In the NEB calculations, energy-weighted spring constants scaling from lower-bound of 0.01 au to an upper-bound of 0.2 au were used.[58] The convergence thresholds of 0.002 and 0.001 au for the maximum component of the atomic force acting on the climbing image (max(|FCI|)) and the root mean squared atomic force acting on the CI (RMS(FCI)) were adopted, respectively.

■ ASSOCIATED CONTENT

Supporting Information

The Supporting Information is available free of charge at https://pubs.acs.org/doi/10.1021/acs.inorgchem.5c05933.

Experimental methods, synthetic procedures and characterization of new compounds, photocatalytic water oxidation experiments, kinetic isotope experiments, spectroscopy studies, electrochemical studies, and single-crystal X-ray analysis (PDF)

Illustration of the process in Figure 6 with dibenzofuran (GIF)

Illustration of the process in Figure 6 with dibenzothiophene (GIF)

Illustration of the process in Figure 6 with carbazole (GIF)

Accession Codes

Deposition Numbers 2394636−2394638 contain the supplementary crystallographic data for this paper. These data can be obtained free of charge via the joint Cambridge Crystallographic Data Centre (CCDC) and Fachinformationszentrum Karlsruhe Access Structures service.

AUTHOR INFORMATION

Corresponding Authors

Frank Würthner − *Institut für Organische Chemie & Center for Nanosystems Chemistry (CNC), Universität Würzburg, 97074 Würzburg, Germany;* orcid.org/0000-0001-7245-0471; Email: frank.wuerthner@uni-wuerzburg.de

Sandra Luber − *Department of Chemistry, University of Zürich, 8057 Zürich, Switzerland;* orcid.org/0000-0002-6203-9379; Email: sandra.luber@chem.uzh.ch

Authors

Gourab Das − *Institut für Organische Chemie & Center for Nanosystems Chemistry (CNC), Universität Würzburg, 97074 Würzburg, Germany*

Daniel A. P. Friedewald − *Institut für Organische Chemie & Center for Nanosystems Chemistry (CNC), Universität Würzburg, 97074 Würzburg, Germany*

Deqi Tang − *Department of Chemistry, University of Zürich, 8057 Zürich, Switzerland*

Kazutaka Shoyama − *Institut für Organische Chemie & Center for Nanosystems Chemistry (CNC), Universität Würzburg, 97074 Würzburg, Germany;* orcid.org/0000-0003-0937-4431

Fabrizio Creazzo − *Department of Chemistry, University of Zürich, 8057 Zürich, Switzerland;* orcid.org/0000-0002-8099-8338

Complete contact information is available at:
https://pubs.acs.org/10.1021/acs.inorgchem.5c05933

Author Contributions

F.W. initiated and supervised the overall project. Synthesis, NMR studies, spectroscopy studies, characterization of the catalytic properties and the growth of the single crystals for crystallographic analysis were performed by G.D. D.A.P.F. carried out electrochemical and NMR studies. The crystallographic measurements and analysis were conducted by K.S. DFT calculations were carried out by D.T. under the supervision of F.C. and S.L. All the authors have contributed to writing the manuscript and have given approval to the final version of the manuscript.

Notes

The authors declare no competing financial interest.

ACKNOWLEDGMENTS

This project has received funding from the European Research Council (ERC) under the European Union's Horizon 2020 research and innovation program (grant agreement no.787937; recipient F.W.). We acknowledge DESY (Hamburg, Germany), a member of the Helmholtz Association HGF, for the provision of experimental facilities. Parts of this research were carried out at PETRA III and we would like to thank Dr. Johanna Hakanpää and Dr. Spyros Chatziefthymiou for assistance in using P11. Beamtime was allocated for proposals I-20220939 and I-20230262. We also acknowledge the University of Zurich for supporting the research and Swiss National Supercomputing Center for providing computational resources under the project ID: s1216.

REFERENCES

(1) Abbass, K.; Qasim, M. Z.; Song, H.; Murshed, M.; Mahmood, H.; Younis, I. A Review of the Global Climate Change Impacts, Adaptation, and Sustainable Mitigation Measures. *Environ. Sci. Pollut. Res.* **2022**, *29*, 42539−42559.

(2) Jacobson, M. Z. Review of solutions to Global Warming, air pollution, and energy security. *Energy Environ. Sci.* **2009**, *2*, 148−173.

(3) Ang, T.-Z.; Salem, M.; Kamarol, M.; Das, H. S.; Nazari, M. A.; Prabaharan, N. A. Comprehensive Study of Renewable Energy Sources: Classifications, Challenges and Suggestions. *Energy Strat. Rev.* **2022**, *43*, No. 100939.

(4) Erdiwansyah; Mahidin; Husin, H.; Nasaruddin; Zaki, M.; Muhibbuddin. A Critical Review of the Integration of Renewable Energy Sources with Various Technologies. *Prot. Control Mod. Power Syst.* **2021**, *6*, 3.

(5) An, Y.; Lin, C.; Dong, C.; Wang, R.; Hao, J.; Miao, J.; Fan, X.; Min, Y.; Zhang, K. Scalable Photoelectrochemical Cell for Overall Solar Water Splitting into H_2 and H_2O_2. *ACS Energy Lett.* **2024**, *9*, 1415−1422.

(6) Hussein, R.; Graça, A.; Forsman, J.; Aydin, A. O.; Hall, M.; Gaetcke, J.; Chernev, P.; Wendler, P.; Dobbek, H.; Messinger, J.; Zouni, A.; Schröder, W. P. Cryo−electron Microscopy Reveals Hydrogen Positions and Water Networks in Photosystem II. *Science* **2024**, *384*, 1349−1355.

(7) Lubitz, W.; Chrysina, M.; Cox, N. Water Oxidation in Photosystem II. *Photosyn. Res.* **2019**, *142*, 105−125.

(8) Umena, Y.; Kawakami, K.; Shen, J. R.; Kamiya, N. Crystal Structure of Oxygen-evolving Photosystem II at a Resolution of 1.9 Å. *Nature* **2011**, *473*, 55−60.

(9) Dismukes, G. C.; Brimblecombe, R.; Felton, G. A. N.; Pryadun, R. S.; Sheats, J. E.; Spiccia, L.; Swiegers, G. F. Development of Bioinspired Mn_4O_4−Cubane Water Oxidation Catalysts: Lessons from Photosynthesis. *Acc. Chem. Res.* **2009**, *42*, 1935−1943.

(10) Loll, B.; Kern, J.; Saenger, W.; Zouni, A.; Biesiadka, J. Towards Complete Cofactor Arrangement in the 3.0 Å Resolution Structure of Photosystem II. *Nature* **2005**, *438*, 1040−1044.

(11) Ferreira, K. N.; Iverson, T. M.; Maghlaoui, K.; Barber, J.; Iwata, S. Architecture of the Photosynthetic Oxygen-Evolving Centre. *Science* **2004**, *303*, 1831−1838.

(12) Gathmann, S. R.; Bartel, C. J.; Grabow, L. C.; Abdelrahman, O. A.; Frisbie, C. D.; Dauenhauer, P. J. Dynamic Promotion of the Oxygen Evolution Reaction via Programmable Metal Oxides. *ACS Energy Lett.* **2024**, *9*, 2013−2023.

(13) Matheu, R.; Garrido-Barros, P.; Gil-Sepulcre, M.; Ertem, M. Z.; Sala, X.; Gimbert-Suriñach, C.; Llobet, A. The Development of Molecular Water Oxidation Catalysts. *Nat. Rev. Chem.* **2019**, *3*, 331−341.

(14) Wu, X.; Liu, X.; Ni, K.; Wen, B.; Guo, R.; Niu, C.; Meng, J.; Li, Q.; Wu, P.; Zhu, Y.; Mai, L. Deep Reconstruction of Nickel-Based Precatalysts for Water Oxidation Catalysis. *ACS Energy Lett.* **2019**, *4*, 2585−2592.

(15) Karkas, M. D.; Verho, O.; Johnston, E. V.; Âkermark, B. Artificial Photosynthesis: Molecular Systems for Catalytic Water Oxidation. *Chem. Rev.* **2014**, *114*, 11863−12001.

(16) Llobet, A. *Molecular Water Oxidation Catalysis*; John Wiley & Sons Ltd.: New York, 2014.

(17) Ghosh, T.; Maayan, G. Efficient Homogeneous Electrocatalytic Water Oxidation by a Manganese Cluster with an Overpotential of Only 74 mV. *Angew. Chem. Int. Ed* **2019**, *58*, 2785−2790. *Angew. Chem.* **2019**, *131*, 2811−2816.

(18) Naruta, Y.; Sasayama, M.-a.; Sasaki, T. Oxygen Evolution by Oxidation of Water with Manganese Porphyrin Dimers. *Angew. Chem. Int. Ed.* **1994**, *33*, 1839−1841.

(19) Gersten, S. W.; Samuels, G. J.; Meyer, T. J. Catalytic Oxidation of Water by an Oxo-bridge Ruthenium Dimer. *J. Am. Chem. Soc.* **1982**, *104*, 4029−4030.

(20) Noll, N.; Würthner, F. Bioinspired Water Preorganization in Confined Space for Efficient Water Oxidation Catalysis in Metal-

losupramolecular Ruthenium Architectures. *Acc. Chem. Res.* **2024**, *57*, 1538−1549.

(21) Matheu, R.; Ertem, M. Z.; Gimbert-Suriñach, G.; Sala, X.; Llobet, A. Seven Coordinated Molecular Ruthenium−Water Oxidation Catalysts: A Coordination Chemistry Journey. *Chem. Rev.* **2019**, *119*, 3453−3471.

(22) Kunz, V.; Schmidt, D.; Röhr, M. I. S.; Mitrić, R.; Würthner, F. Supramolecular Approaches to Improve the Performance of Ruthenium-Based Water Oxidation Catalysts. *Adv. Energy Mater.* **2017**, *7*, No. 1602939.

(23) Duan, L.; Wang, L.; Li, F.; Li, F.; Sun, L. Highly Efficient Bioinspired Molecular Ru Water Oxidation Catalysts with Negatively Charged Backbone Ligands. *Acc. Chem. Res.* **2015**, *48*, 2084−2096.

(24) López, I.; Ertem, M. Z.; Maji, S.; Benet-Buchholz, J.; Keidel, A.; Kuhlmann, U.; Hildebrandt, P.; Cramer, C. J.; Batista, V. S.; Llobet, A. A Self-Improved Water-Oxidation Catalyst: Is One Site Really Enough? *Angew. Chem. Int. Ed* **2014**, *53*, 205−209. *Angew. Chem.* **2014**, *126*, 209−213.

(25) Kaveevivitchai, N.; Chitta, R.; Zong, R.; El Ojaimi, M.; Thummel, R. P. A Molecular Light-Driven Water Oxidation Catalyst. *J. Am. Chem. Soc.* **2012**, *134*, 10721−10724.

(26) Zong, R.; Thummel, R. P. A New Family of Ru Complexes for Water Oxidation. *J. Am. Chem. Soc.* **2005**, *127*, 12802−12803.

(27) Zhang, B.; Sun, L. Ru-bda: Unique Molecular Water-Oxidation Catalysts with Distortion Induced Open Site and Negatively Charged Ligands. *J. Am. Chem. Soc.* **2019**, *141*, 5565−5580.

(28) Duan, L.; Bozoglian, F.; Mandal, S.; Stewart, B.; Privalov, T.; Llobet, A.; Sun, L. A Molecular Ruthenium Catalyst with Water-Oxidation Activity Comparable to that of Photosystem II. *Nat. Chem.* **2012**, *4*, 418−423.

(29) Duan, L.; Fischer, A.; Xu, Y.; Sun, L. Isolated Seven-Coordinate Ru(IV) Dimer Complex with [HOHOH]− Bridging Ligand as an Intermediate for Catalytic Water Oxidation. *J. Am. Chem. Soc.* **2009**, *131*, 10397−10399.

(30) Das, B.; Rahaman, A.; Shatskiy, A.; Verho, O.; Kärkäs, M. D.; Åkermark, B. The Impact of Ligand Carboxylates on Electrocatalyzed Water Oxidation. *Acc. Chem. Res.* **2021**, *54*, 3326−3337.

(31) Vereshchuk, N.; Holub, J.; Gil-Sepulcre, M.; Benet-Buchholz, J.; Llobet, A. Fate of the Molecular Ru−Phosphonate Water Oxidation Catalyst under Turnover Conditions. *ACS Catal.* **2021**, *11*, 5240−5247.

(32) Muckerman, J. T.; Kowalczyk, M.; Badiei, Y. M.; Polyansky, D. E.; Concepcion, J. J.; Zong, R.; Thummel, R. P.; Fujita, E. New Water Oxidation Chemistry of a Seven-Coordinate Ruthenium Complex with a Tetradentate Polypyridyl Ligand. *Inorg. Chem.* **2014**, *53*, 6904−6913.

(33) Liu, T.; Li, G.; Shen, N.; Wang, L.; Timmer, B. J. J.; Kravchenko, A.; Zhou, S.; Gao, Y.; Yang, Y.; Yang, H.; Xu, B.; Zhang, B.; Ahlquist, M. S. G.; Sun, L. Promoting Proton Transfer and Stabilizing Intermediates in Catalytic Water Oxidation via Hydrophobic Outer Sphere Interactions. *Chem.—Eur. J.* **2022**, *28*, No. e202104562.

(34) Matheu, R.; Ertem, M. Z.; Pipelier, M.; Lebreton, J.; Dubreuil, D.; Benet-Buchholz, J.; Sala, X.; Tessier, A.; Llobet, A. The Role of Seven-Coordination in Ru-Catalyzed Water Oxidation. *ACS Catal.* **2018**, *8*, 2039−2048.

(35) Matheu, R.; Ertem, M. Z.; Gimbert-Suriñach, C.; Benet-Buchholz, J.; Sala, X.; Llobet, A. Hydrogen Bonding Rescues Overpotential in Seven-Coordinated Ru Water Oxidation Catalysts. *ACS Catal.* **2017**, *7*, 6525−6532.

(36) Maji, S.; López, I.; Bozoglian, F.; Benet-Buchholz, J.; Llobet, A. Mononuclear Ruthenium−Water Oxidation Catalysts: Discerning between Electronic and Hydrogen-Bonding Effects. *Inorg. Chem.* **2013**, *52*, 3591−3593.

(37) Noll, N.; Groß, T.; Shoyama, K.; Beuerle, F.; Würthner, F. Folding-Induced Promotion of Proton-Coupled Electron Transfers via Proximal Base for Light-Driven Water Oxidation. *Angew. Chem., Int. Ed.* **2023**, *62*, No. e202217745.

(38) Kunz, V.; Schulze, M.; Schmidt, D.; Würthner, F. Trinuclear Ruthenium Macrocycles: Toward Supramolecular Water Oxidation Catalysis in Pure Water. *ACS Energy Lett.* **2017**, *2*, 288−293.

(39) Schulze, M.; Kunz, V.; Frischmann, P. D.; Würthner, F. A Supramolecular Ruthenium Macrocycle with High Catalytic Activity for Water Oxidation that Mechanistically Mimics Photosystem II. *Nat. Chem.* **2016**, *8*, 576−583.

(40) Noll, N.; Krause, A.-M.; Beuerle, F.; Würthner, F. Enzyme-Like Water Preorganization in a Synthetic Molecular Cleft for Homogeneous Water Oxidation Catalysis. *Nat. Catal.* **2022**, *5*, 867−877.

(41) Liu, T.; Li, G.; Shen, N.; Wang, L.; Timmer, B. J. J.; Zhou, S.; Zhang, B.; Kravchenko, A.; Xu, B.; Ahlquist, M. S. G.; Sun, L. Isolation and Identification of Pseudo Seven-Coordinate Ru(III) Intermediate Completing the Catalytic Cycle of Ru-bda Type of Water Oxidation Catalysts. *CCS Chem.* **2022**, *4*, 2481−2490.

(42) Osswald, P.; Würthner, F. Effects of Bay Substituents on the Racemization Barriers of Perylene Bisimides: Resolution of Atropo-Enantiomers. *J. Am. Chem. Soc.* **2007**, *129*, 14319−14326.

(43) Zhan, S.; Zhang, B.; Sun, L.; Ahlquist, M. S. G. Hydrophobic/Hydrophilic Directionality Affects the Mechanism of Ru-Catalyzed Water Oxidation Reaction. *ACS Catal.* **2020**, *10*, 13364−13370.

(44) Becke, A. D. Density-functional Exchange-energy Approximation with Correct Asymptotic Behaviour. *Phys. Rev. A* **1988**, *38*, 3098−3100.

(45) Lee, C.; Yang, W.; Parr, R. G. Development of the Colle-Salvetti Correlation-energy Formula into a Functional of the Electron Density. *Phys. Rev. B* **1988**, *37*, 785−789.

(46) Becke, A. D. Density-functional Thermochemistry. III. The Role of Exact Exchange. *J. Chem. Phys.* **1993**, *98*, 5648−5652.

(47) Stukowski, A. Visualization and Analysis of Atomistic Simulation Data with OVITO−the Open Visualization Tool. *Modelling Simul. Mater. Sci. Eng.* **2010**, *18*, No. 015012.

(48) Kabsch, W. XDS. *Acta Crystallogr. Sect. D* **2010**, *66*, 125−132.

(49) Sheldrick, G. M. SHELXT − Integrated Space-Group and Crystal-Structure Determination. *Acta Crystallogr., Sect. A* **2015**, *71*, 3−8.

(50) Sheldrick, G. M. Crystal Structure Refinement with SHELXL. *Acta Crystallogr. Sect. C* **2015**, *71*, 3−8.

(51) Spek, A. L. Platon Squeeze: A Tool for the Calculation of the Disordered Solvent Contribution to the Calculated Structure Factors. *Acta Crystallogr. C* **2015**, *71*, 9−18.

(52) Spek, A. L. Structure Validation in Chemical Crystallography. *Acta Crystallogr. Sect. D* **2009**, *65*, 148−155.

(53) Spek, A. L. CheckCIF Validation ALERTS: What They Mean and How to Respond. *Acta Crystallogr. E* **2020**, *76*, 1−11.

(54) Kunz, V.; Lindner, J. O.; Schulze, M.; Röhr, M. I. S.; Schmidt, D.; Mitrić, R.; Würthner, F. Cooperative Water Oxidation Catalysis in a Series of Trinuclear Metallosupramolecular Ruthenium Macrocycles. *Energy Environ. Sci.* **2017**, *10*, 2137−2153.

(55) Meza-Chincha, A.-L.; Lindner, J. O.; Schindler, D.; Schmidt, D.; Krause, A.-M.; Röhr, M. I. S.; Mitrić, R.; Würthner, F. Impact of Substituents on Molecular Properties and Catalytic Activities of Trinuclear Ru Macrocycles in Water Oxidation. *Chem. Sci.* **2020**, *11*, 7654−7664.

(56) Noll, N.; Würthner, F. A Calix[4]arene-Based Cyclic Dinuclear Ruthenium Complex for Light-Driven Catalytic Water Oxidation. *Chem.—Eur. J.* **2021**, *27*, 444−450.

(57) Carey, F. A.; Sundberg, R. J. *Advanced Organic Chemistry: Part A: Structure and Mechanisms 222−225*; Springer: US, 2007.

(58) Ásgeirsson, V.; Birgisson, B. O.; Bjornsson, R.; Becker, U.; Neese, F.; Riplinger, C.; Jónsson, H. Nudged Elastic Band Method for Molecular Reactions Using Energy-Weighted Springs Combined with Eigenvector Following. *J. Chem. Theory Comput.* **2021**, *17*, 4929−4945.

(59) Henkelman, G.; Uberuaga, B. P.; Jónsson, H. A Climbing Image Nudged Elastic Band Method for Finding Saddle Points and Minimum Energy Paths. *J. Chem. Phys.* **2000**, *113*, 9901−9904.

(60) Neese, F. The ORCA Program System. Wiley. *Interdiscip. Rev. Comput. Mol. Sci.* **2012**, *2*, 73−78.

(61) Neese, F. Software Update: The ORCA Program System—Version 5.0. *Wiley Interdiscip. Rev. Comput. Mol. Sci.* **2022**, *12*, No. e1606.

(62) Grimme, S.; Antony, J.; Ehrlich, S.; Krieg, H. A Consistent and Accurate ab Initio Parametrization of Density Functional Dispersion Correction (DFT-D) for the 94 Elements H-Pu. *J. Chem. Phys.* **2010**, *132*, No. 154104.

(63) Grimme, S.; Ehrlich, S.; Goerigk, L. Effect of the Damping Function in Dispersion Corrected Density Functional Theory. *J. Comput. Chem.* **2011**, *32*, 1456−1465.

(64) Weigend, F.; Ahlrichs, R. Balanced Basis Sets of Split Valence, Triple Zeta Valence and Quadruple Zeta Valence Quality for H to Rn: Design and Assessment of Accuracy. *Phys. Chem. Chem. Phys.* **2005**, *7*, 3297−3305.

(65) Becke, A. D. Density-functional Exchange-energy Approximation with Correct Asymp- totic Behaviour. *Phys. Rev. A* **1988**, *38*, 3098−3100.

(66) Lee, C.; Yang, W.; Parr, R. G. Development of the Colle-Salvetti Correlation-energy Formula into a Functional of the Electron Density. *Phys. Rev. B* **1988**, *37*, 785−789.

(67) Becke, A. D. Density-functional Thermochemistry. III. The Role of Exact Exchange. *J. Chem. Phys.* **1993**, *98*, 5648−5652.

(68) Barone, V.; Cossi, M. Quantum Calculation of Molecular Energies and Energy Gradients in Solution by a Conductor Solvent Model. *J. Phys. Chem. A* **1998**, *102*, 1995−2001.

(69) Stull, J. A.; Stich, T. A.; Hurst, J. K.; Britt, R. D. Electron Paramagnetic Resonance Analysis of a Transient Species Formed During Water Oxidation Catalyzed by the Complex Ion $[(bpy)_2Ru(OH_2)]_2O^{4+}$. *Inorg. Chem.* **2013**, *52*, 4578−4586.

(70) Daniel, Q.; Huang, P.; Fan, T.; Wang, Y.; Duan, L.; Wang, L.; Li, F.; Rinkevicius, Z.; Mamedov, F.; Ahlquist, M. S. G.; Styring, S.; Sun, L. Rearranging from 6- to 7-Coordination Initiates the Catalytic Activity: An EPR Study on a Ru-bda Water Oxidation Catalyst. *Coord. Chem. Rev.* **2017**, *346*, 206−215.

(71) Li, G.; Ahlquist, M. S. G. Computational Comparison of $Ru(bda)(py)_2$ and $Fe(bda)(py)_2$ as Water Oxidation Catalysts. *Dalton Trans.* **2022**, *51*, 8618−8624.